

Hydra: an Ensemble of Convolutional Neural Networks for Geospatial Land Classification

Rodrigo Minetto, Maurício Pamplona Segundo, Sudeep Sarkar

Abstract—We describe in this paper Hydra, an ensemble of convolutional neural networks (CNN) for geospatial land classification. The idea behind Hydra is to create an initial CNN that is coarsely optimized but provides a good starting pointing for further optimization, which will serve as the Hydra’s body. Then, the obtained weights are fine tuned multiple times to form an ensemble of CNNs that represent the Hydra’s heads. By doing so, we were able to reduce the training time while maintaining the classification performance of the ensemble. We created ensembles using two state-of-the-art CNN architectures, ResNet and DenseNet, to participate in the Functional Map of the World challenge. With this approach, we finished the competition in third place. We also applied the proposed framework to the NWPU-RESISC45 database and achieved the best reported performance so far. Code and CNN models are available at <https://github.com/maups/hydra-fmow>.

Index Terms—Geospatial land classification, remote sensing image classification, functional map of world, ensemble learning, on-line data augmentation, convolutional neural network.



1 INTRODUCTION

Land use is a critical piece of information for a wide range of applications, from humanitarian to military purposes. For this reason, automatic land use classification from satellite images has been drawing increasing attention from academia, industry and government agencies. One of the most recent initiatives in this area is the Functional Map of the World (FMOW) challenge [1] sponsored by the Intelligence Advanced Research Projects Activity (IARPA), an organization within the Office of the USA Director of National Intelligence.

The FMOW challenge consists of creating automatic solutions to classify a specific given location as one of the 62 target classes (*e.g.* airport, flooded road, nuclear power plant and so on) or as none of them (false detections). FMOW images vary in quality and are distributed over more than 100,000 globe locations, which leads to high intraclass variations and considerable interclass confusion. This, added to traditional satellite imaging problems like viewpoint, weather, shadow and scale variations, makes this classification problem a lot harder than previous land use datasets, such as UC Merced Land Use Dataset [2], WHU-RS19 [3] and NWPU-RESISC45 [4]. Finally, the FMOW challenge also limits time and computational resources for training and testing to minimize the disparity among participants’ solutions.

To cope with the difficulties and restrictions of the FMOW challenge, as our main contribution, in this work

we present a framework that creates ensembles of Convolutional Neural Networks (CNN) for land use classification in satellite images, which we called Hydra. The idea behind Hydra is to create an initial CNN that is coarsely optimized but provides a good starting pointing for further optimization, which will serve as the Hydra’s body. Then, the obtained weights are fine tuned multiple times to form an ensemble of CNNs that represent the Hydra’s heads. The Hydra framework tackles one of the most common problem in multiclass classification, which is the existence of several local minima that prioritize some classes over others and the eventual absence of a global minimum within the classifier search space. The ensemble ends up expanding this space by combining multiple classifiers that converged to local minima and reaches a better global approximation. Figure 1 illustrates this process, where a black line represents the body optimization part and the red lines represent the heads reaching different local minima. To stimulate convergence to different end points, we exploit different strategies, such as using online data augmentation, variations in the size of the region of interest, and different image formats released by FMOW.

2 THE FMOW CHALLENGE

The main goal of the FMOW challenge was to encourage researchers and machine learning experts to design automatic classification solutions for land use interpretation in satellite images. The competition was hosted by Top-Coder¹, where participants had one submission every three hours to keep track of their ongoing performance. Details regarding dataset, scoring, and restrictions are given in Sections 2.1, 2.2, and 2.3, respectively.

1. <https://www.topcoder.com/>

- R. Minetto is with Universidade Tecnológica Federal do Paraná (UTFPR), Brazil. E-mail: rodrigo.minetto@gmail.com
- M. P. Segundo is with Universidade Federal da Bahia (UFBA), Brazil. E-mail: mauriciops@ufba.br
- S. Sarkar is with Department of Computer Science and Engineering, University of South Florida (USF), Tampa, FL, USA. E-mail: sarkar@usf.edu
- The research in this paper was conducted while the authors were at the Computer Vision and Pattern Recognition Group, USF.

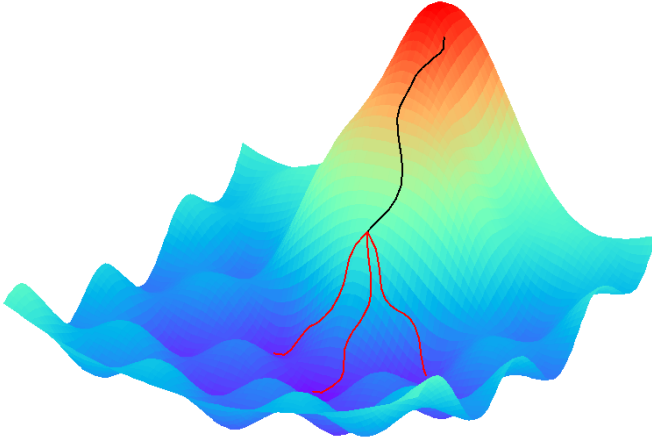


Fig. 1. Illustration of the optimization process in the Hydra framework. The black line represents the coarse parameter optimization that forms the Hydra’s body. The red lines represent the Hydra’s heads, which are obtained after fine tuning the body parameters multiple times seeking to reach different local minima.

2.1 Dataset

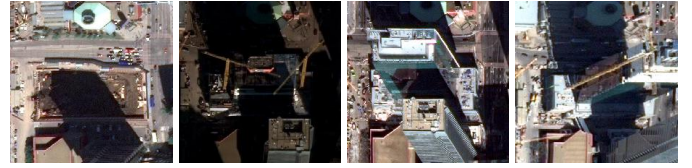
The FMOW dataset, as detailed by Christie *et al.* [1], contains almost half of a million images split into training, evaluation and testing subsets, as presented in Table 1. It was publicly released² in two image formats: JPEG (194 GB) and TIFF (2.8 TB). For both formats, high-resolution pan-sharpened [5] and multi-spectral images were available, although the latter one varies with the format. While TIFF images provided the original 4/8-band multi-spectral information, the color space was compressed in JPG images to fit their 3-channel limitation.

TABLE 1
Table of contents of the FMOW dataset.

| | # of images | # of boxes | # of distinct boxes |
|--------------|----------------|----------------|---------------------|
| Training | 363,572 | 363,572 | 83,412 |
| Evaluation | 53,041 | 63,422 | 12,006 |
| Testing | 53,473 | 76,988 | 16,948 |
| Total | 470,086 | 503,982 | 112,366 |

Pan-sharpened image dimensions range from 293×230 to 16184×16288 pixels, and multi-spectral from 74×58 to 4051×4077 . Each image has one or more annotated boxes that correspond to regions of interest. Some of these regions may appear in several images taken in different time periods, adding a temporal element to the problem, as shown in Figures 2(a) and 2(b). Traditional problems arising from that include, but are not limited to, variations in shadows, satellite viewpoint and weather conditions. Figures 2(c) and 2(d) illustrate other recurrent problems in the FMOW dataset: inaccurate annotations and large variations in region size.

Each region is an instance of one of the 62 classes or a false detection. All classes considered in the FMOW challenge are illustrated in Figure 3. Those classes have an unbalanced distribution, as shown in Figure 4. Images in the training subset contain a single region that is never a



(a)



(b)



(c)



(d)

Fig. 2. Different challenges in FMOW satellite images: (a) shadow and viewpoint variations, (b) arbitrary weather conditions, (c) inaccurate annotations and (d) scale variations.

false detection. The evaluation subset has images with one or two regions, with at least one not being a false detection. Testing images may have several regions but their labels are unknown (see Figure 2(d)). From 53,473 images in the test subset, 82.60% have a single region, 4.96% have two regions, 5.66% have three regions and 6.78% have four regions or more, with a maximum number of fourteen regions per image.

The FMOW dataset also provides different metadata along with each region, such as bounding box and image size, ground sample distance, region visibility, cloud cover, timestamps, wavelengths, scan direction, sun elevation, Universal Transverse Mercator (UTM) zone, and so on.

2.2 Scoring

Submissions consisted of a list with one label prediction — among the m possible classes ($m = 63$, *i.e.* 62 land use classes plus false detection) — for each distinct region in the test set. When the same region appeared in several images, like the ones in Figures 2(a) and 2(b), the competitors were asked to merge all these information into a single label outcome. The quantitative criteria used by the FMOW challenge to rank its competitors was a weighted average of the F -measure [6] for each class.

2. <https://www.iarpa.gov/challenges/fmow.html>

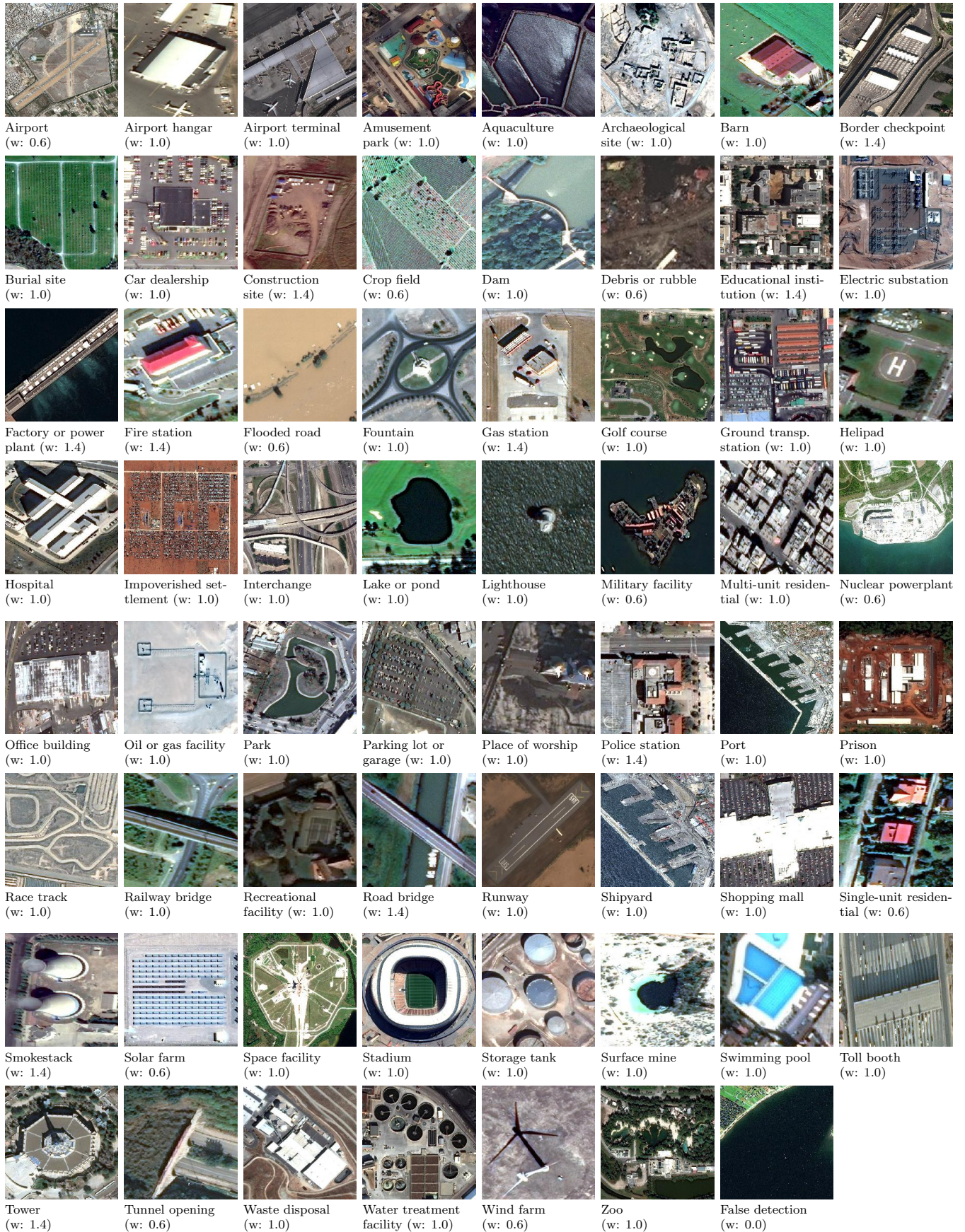


Fig. 3. List of classes of the FMOW challenge. An image example, a label and an associated weight are presented for each class. The least challenging classes have a lower weight (0.6) while the most difficult ones have a higher weight (1.4). These weights impact the final classification score.

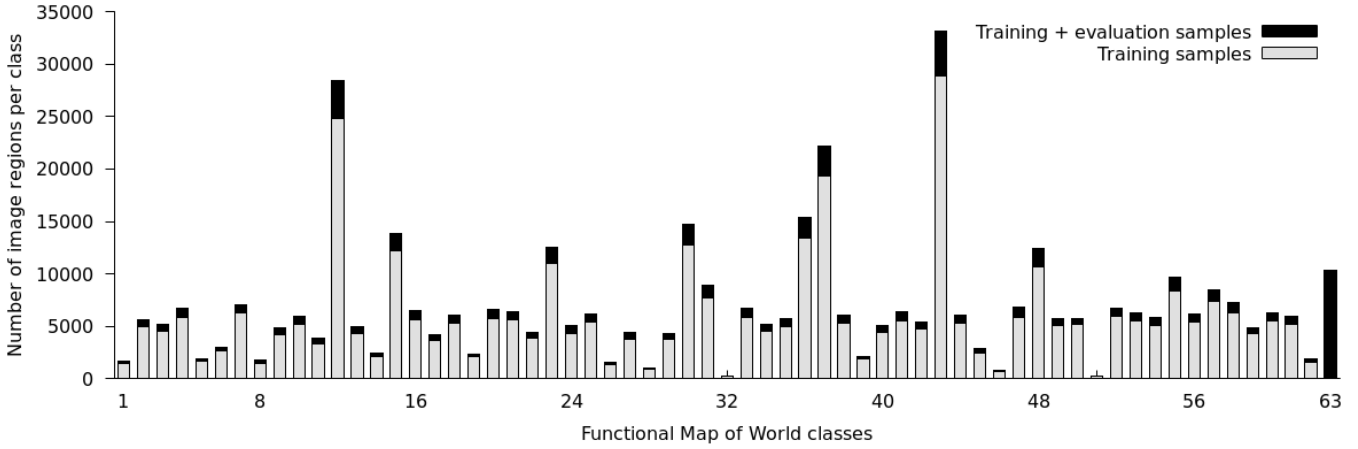


Fig. 4. The class histogram distribution for the training (gray bars) and evaluation sets (black bars) by using the 3-band pansharpened JPEG/RGB set. Note the highly unbalanced class distribution.

Let $P = \langle e_1, e_2, \dots, e_n \rangle$ be the predicted labels provided by a competitor and $G = \langle g_1, g_2, \dots, g_n \rangle$ the ground-truth labels for n distinct test regions. From P and G , one can derive a confusion matrix C :

| | | Predicted label | | | |
|--------------------|-----------|-----------------|-------------|-----|-------------|
| | | class 1 | class 2 | ... | class m |
| Ground-truth label | class 1 | $C_{1,1}$ | $C_{1,2}$ | ... | $C_{1,m}$ |
| | class 2 | $C_{2,1}$ | $C_{2,2}$ | ... | $C_{2,m}$ |
| | ⋮ | ⋮ | ⋮ | ⋮ | ⋮ |
| | class m-1 | $C_{m-1,1}$ | $C_{m-1,2}$ | ... | $C_{m-1,m}$ |
| | class m | $C_{m,1}$ | $C_{m,2}$ | ... | $C_{m,m}$ |

where $C_{i,i}$ is the number of correct classifications for the i -th class and $C_{i,j}$ the number of images from the i -th class that were mistakenly classified as the j -th class. With these values we compute the precision P_i and recall R_i scores for the i -th class as follows:

$$P_i = \frac{tp_i}{tp_i + fp_i} \quad R_i = \frac{tp_i}{tp_i + fn_i}$$

where:

$$tp_i = C_{i,i} \quad fp_i = \sum_{j=1, j \neq i}^m C_{j,i} \quad fn_i = \sum_{j=1, j \neq i}^m C_{i,j}$$

are respectively the number of true positives, false positives and false negatives for the i -th class. The F -measure for each class is then computed as the harmonic mean of precision and recall:

$$F_i = \frac{2 \times P_i \times R_i}{P_i + R_i}$$

The final score \bar{F} is the weighted sum of the F -measure for all classes:

$$\bar{F} = \frac{\sum_{i=1}^m F_i \times w_i}{\sum_{i=1}^m w_i} \quad (1)$$

where w_i is the weight of i -th class. The weights for each class are provided in Figure 3. It is worth noting that the weight for false detections is 0, but it does not mean it will not affect \bar{F} . If a region is misclassified as a false detection, its class will have an additional false negative. If a false detection is misclassified as another class, one more false positive will be taken into account.

2.3 Hardware and time restrictions

The competition ran from September 21st to December 31st, 2017. The provisional standings were used to select the top 10 competitors as finalists. For the final round, competitors were asked to provide a dockerized version³ of their solutions, and the final standings were determined based on the results for a separate sequestered dataset (*i.e.* none of the competitors had access to these images). The dockerized solution had to cope with the following limitations:

- All models required by the solution should be generated during training using raw data only (*i.e.* pre-processed data was not allowed) within 7 days.
- The prediction for all test images should be performed in no more than 24 hours. Prebuilt models should be provided to enable testing before training.
- Hardware was restricted to two types of Linux AWS instances: *m4.10xlarge* and *g3.16xlarge*.

Instances of the type *m4.10xlarge* have 40 Intel Xeon E5-2686 v4 (Broadwell) processors and 160GB of memory and were recommended for CPU-based systems. Instances of the type *g3.16xlarge* have 4 NVIDIA Tesla M60 GPUs, 64 similar processors and 488GB of memory and were recommended for GPU-based systems. However, as can be noticed, a *g3.16xlarge* instance was best suited for both CPU-based and GPU-based systems.

3. <https://www.docker.com/>

2.4 Baseline

The organizers released a baseline classification code⁴ in October 14th, 2017, and updated that solution in November 17th of the same year. The most recent and accurate version of the baseline consists in extracting discriminant features from images and metadata using deep neural networks. To this end, they concatenated image features obtained by a CNN (DenseNet-161 [7]) to a preprocessed vector of metadata (mean subtraction) and fed this to a multilayer perceptron (MLP) with 2 hidden layers. A softmax loss is then used by the Adam optimizer [8] during training. They used both training and validation subsets for training, and no augmentation was performed. More details can be found in the work of Christie *et al.* [1]. The classifiers employed in our Hydra framework are variations of this baseline code.

3 THE HYDRA FRAMEWORK

Ensembles of learning algorithms have been effectively used to improve the classification performance in many computer vision problems [9], [10], [11]. The reasons for that, as pointed out by Dietterich [12] are: the training phase could not provide sufficient data to build a single best classifier; the optimization algorithm fails to converge to the global minimum, but an ensemble using distinct starting points could better approximate the optimal result; or the space being searched may not contain the optimal global minimum, but an ensemble may expand this space for a better approximation.

Formally, a supervised machine learning algorithm receives a list of training samples $\{(x_1, y_1), (x_2, y_2), \dots, (x_m, y_m)\}$ drawn from some unknown function $y = f(x)$ — where x is the feature vector and y the class — and searches for a function h through a space of functions \mathcal{H} , also known as hypotheses, that best matches y . As described by Dietterich [12], an ensemble of learning algorithms build a set of hypotheses $\{h_1, h_2, \dots, h_k\} \in \mathcal{H}$ with respective weights $\{w_1, w_2, \dots, w_k\}$, and then provides a classification decision \bar{y} through hypotheses fusion. Different fusion approaches may be exploited, such as weighted sum $\bar{y} = \sum_{i=1}^k w_i h_i(x)$, majority voting, and so on.

Hydra is a framework to create ensembles of CNNs. As pointed out by Sharkey [13], a neural network ensemble can be build by: varying the initial weights; varying the network architecture; and varying the training set. Varying the initial weights, however, requires a full optimization for each starting point and thus consumes too much computational resources. For the same reason, varying the network architecture demands caution when it is not possible to share learned information between different architectures. Unlike previous possibilities, varying the training set can be done in any point of the optimization process for one or multiple network architectures, and, depending on how it is done, it may not impact the final training cost.

Our framework uses two state-of-the-art CNN architectures, *ResNet* [14] and *DenseNet* [7], as shown in Figures 5 and 6. The training process depicted in Figure 5 consists in first creating the body of the Hydra by coarsely optimizing the chosen architectures using weights pretrained

on IMAGENET [15] as a starting point. Then, the obtained weights serve as starting point for several copies of these CNNs, which are further optimized to form the heads of the Hydra. During testing, an image is fed to all Hydra’s heads and their outputs are fused to generate a single decision, as illustrated in Figure 6.

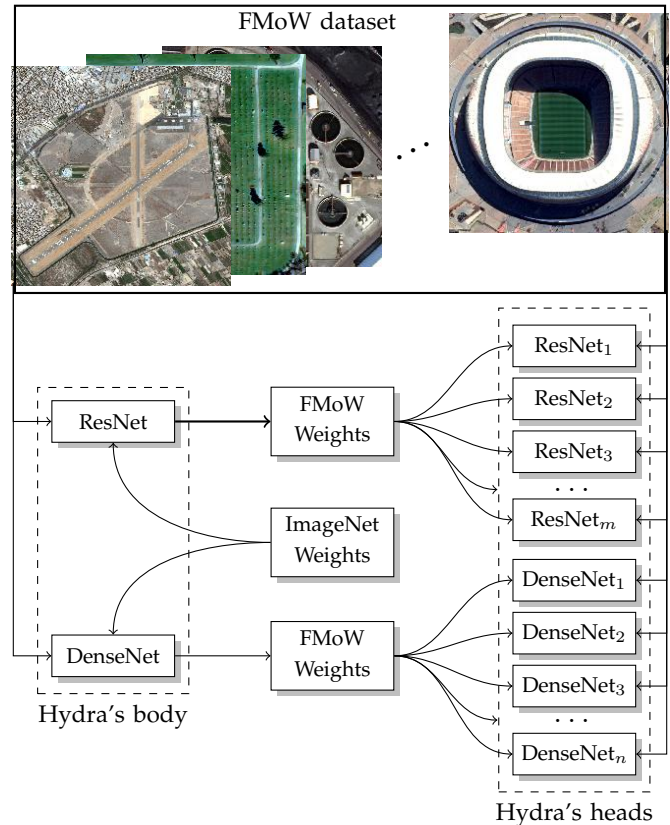


Fig. 5. Hydra’s training flowchart: two CNNs, ResNet and DenseNet, are optimized starting from the ImageNet weights to create the Hydra’s body. The obtained weights are then used as starting point for several copies of these CNNs, which are further optimized to form the heads of the Hydra.

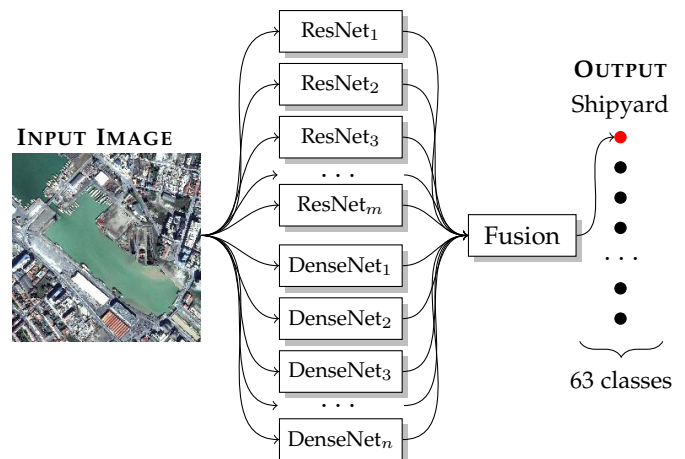


Fig. 6. Hydra’s inference flowchart: an input image is fed to all heads of the Hydra, and each head outputs the probability of each class being the correct one. A majority voting is then used to determine the final label, considering that each head votes for its most probable label.

4. <https://github.com/fmow/baseline>

A key point on ensemble learning, as observed by Krogh *et al.* [16] and Xandra *et al.* [17], is that the hypotheses should be as accurate and as diverse as possible. In Hydra, such properties were prompted by applying different geometric transformations over the training samples, like zoom, shift, reflection and rotations. More details regarding the proposed framework are presented in Sections 3.1, 3.2 and 3.3.

3.1 CNN architectures

Both CNN architectures used in this work, ResNet (ResNet-50) [14] and DenseNet (DenseNet-161) [7], were chosen for achieving state-of-the-art results in different classification problems while being complementary to each other. Let $\mathcal{F}_\ell(\cdot)$ a non-linear transformation — a composite function of convolution, relu, pooling, batch normalization and so on — for layer ℓ . As described by He *et al.* [14], a ResNet unit can be defined as:

$$x_\ell = \mathcal{F}_\ell(x_{\ell-1}) + x_{\ell-1} \quad (2)$$

where $x_{\ell-1}$ and x_ℓ are the input and output of layer ℓ , and x_0 is the input image. ResNets are built by stacking several of these units, creating bypasses for gradients that improve the back-propagation optimization in very deep networks. As a consequence, ResNets may end up generating redundant layers. As a different solution to improve the flow of gradients in deep networks, Huang *et al.* [7] proposed to connect each layer to all preceding layers, which was named a DenseNet unit:

$$x_\ell = \mathcal{F}_\ell([x_0, x_1, \dots, x_{\ell-1}]) \quad (3)$$

where $[x_0, x_1, \dots, x_{\ell-1}]$ is the concatenation of the ℓ previous layer outputs. DenseNets also stack several units, but they use transition layers to limit the number of connections. In the end, DenseNets have less parameters than ResNets and compensate this facts through feature reuse. This difference in behavior may be one of the causes for their complementarity.

Both networks are initialized with weights from ImageNet [15] and trained for six epochs using the Adam optimization algorithm [8] with a learning rate of 10^{-4} . Fully connected layers with ImageNet weights are discarded, and three new layers with 4096 neurons are trained from scratch using a 50% dropout rate, as illustrated in Figure 7. Any given image metadata that is useful for classification (*e.g.* ground sample distance, sun angle) is concatenated to the input of the first fully connected layer.

The obtained CNN weights from the previous step will then be used as starting point to multiple copies of the chosen networks, which will be trained for five more epochs using progressive drops in the learning rate as follows: a learning rate of 10^{-4} is used for the first epoch, 10^{-5} for the following three epochs, and 10^{-6} for the last epoch.

During training, we added different class weights to the loss function for different heads seeking to enhance the complementarity between them. Four different weighting schemes were used: unweighted classes, FMOW class weights as presented in Figure 3 (false detection weight was set to 1), a frequency-based weighting using the balanced heuristic [18], and a manual adjustment of the latter.

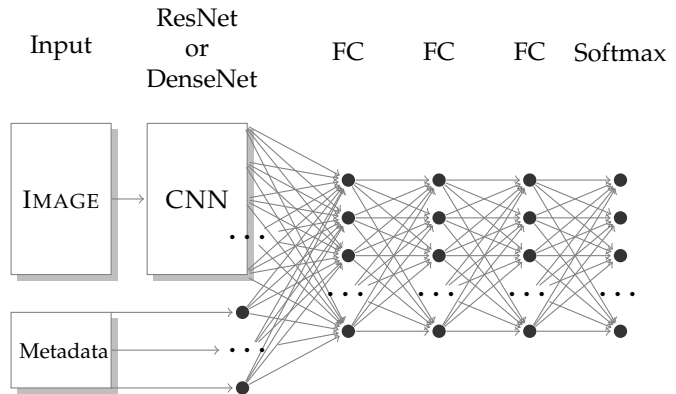


Fig. 7. The convolutional neural network architecture used by the Hydra framework.

3.2 On-line data augmentation

The process of artificially augmenting the image samples in machine learning by using class-preserving transformations is meant to reduce the overfitting in imbalanced classification problems or to improve the generalization ability in the absence of enough data [19], [20], [21], [22], [23]. The breakthroughs achieved by many state-of-the-art algorithms that benefit from data augmentation has lead many authors [24], [25], [26], [27] to study the effectiveness of this technique.

Different techniques can be considered, such as geometric (*e.g.* reflection, scaling, warping, rotation and translation) and photometric (*e.g.* brightness and saturation enhancements, noise perturbation, edge enhancement and color palette changing) transformations. However, as pointed out by Ratner *et al.* [28], selecting transformations and tuning their parameters can be a tricky and time-consuming task. A careless augmentation may produce unrealistic or meaningless images that will negatively affect the performance.

The process of data augmentation can be conducted off-line, as illustrated in Figure 8. In this case, training images undergo geometric and/or photometric transformations before the training. Although this approach avoids repeating the same transformation several times, it also considerably increases the size of the training set. For instance, if we only consider basic rotations (90, 180 and 270 degrees) and reflections, the FMOW training set will have more than 2.8 million samples. This would not only increase the amount of required storage space, but the time consumed by a training epoch as well.

In our framework we apply an on-line augmentation, as illustrated in Figure 9. To this end, different random transformations were applied to the training samples every epoch. This way, the number of transformations seen during training increase with the number of epochs. In addition, different heads of the Hydra experience different versions of the training set and hardly converge to the same local minima.

On-line data augmentations were carried out by the ImageDataGenerator function from Keras⁵. We used random flips in vertical and horizontal directions, random zooming and random shifts over different image crops. We did not use any photometric distortion to avoid creating

5. <https://keras.io/>

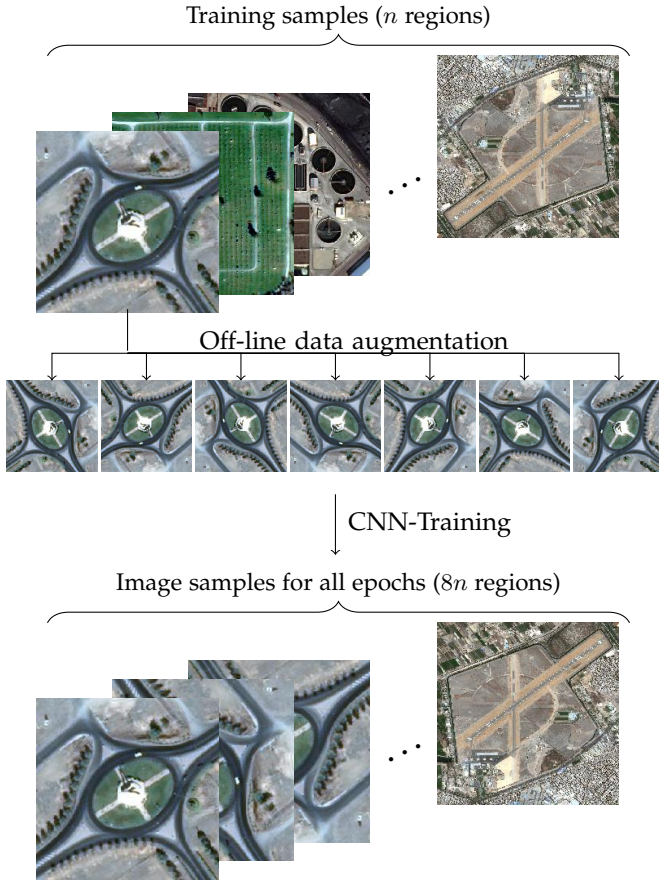


Fig. 8. Illustration of an off-line data augmentation process. In this example considering basic rotations (90, 180 and 270 degrees) and reflections only, each image is augmented to a set of 8 images before the training starts. After that, the augmented training set is static for all CNN epochs.

meaningless training samples. Three image crop styles were considered, as illustrated in Figure 10: the original bounding box that was provided as a metadata (Figure 10(a)), and an expanded bounding box extracted from both JPG pan-sharpened images (Figure 10(b)) and JPG multi-spectral images (Figure 10(c)). As multi-spectral images have low resolution, we discarded samples with less than 96 pixels of width or height. Table 2 presents the configuration of each head in terms of network architecture, augmentation technique and class weighting.

3.3 Fusion and decision

To determine the most appropriate label for an input region according to the models generated by Hydra, we have to combine the results from each head. Each head produces a vector of score values that indicate how well the input region fits each class. As some regions may appear in more than one image, their vectors are summed so that each region ends up with only one vector of scores. The softmax function is then applied to convert these scores to probabilities, and the most probable class is selected for each head. A majority voting is the used to select the final label. However, if the number of votes is below or equal to half of the head count, the region is considered a false detection.

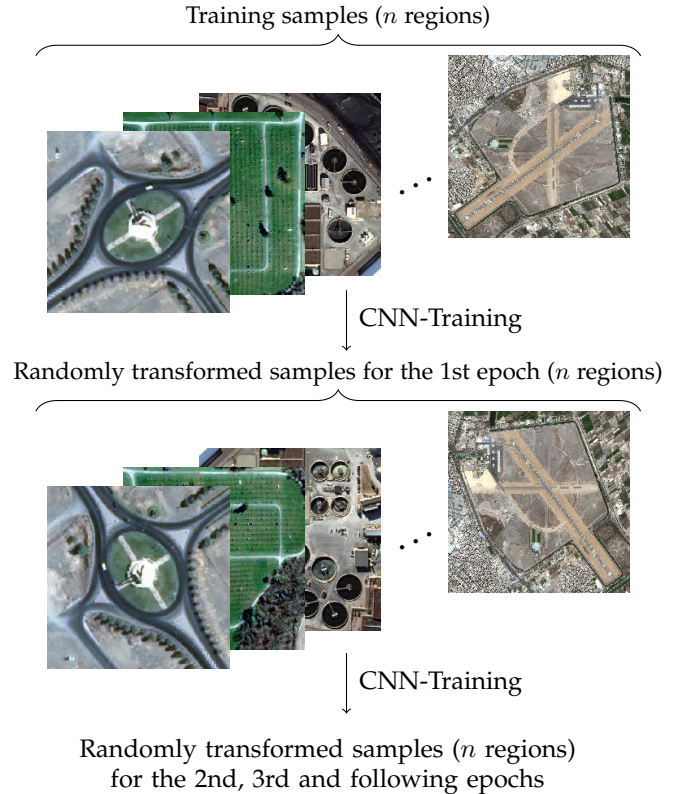


Fig. 9. Illustration of an on-line data augmentation process. In this example considering basic rotations (90, 180 and 270 degrees) and reflections only, each image is randomly transformed into a new image before each training epoch starts.

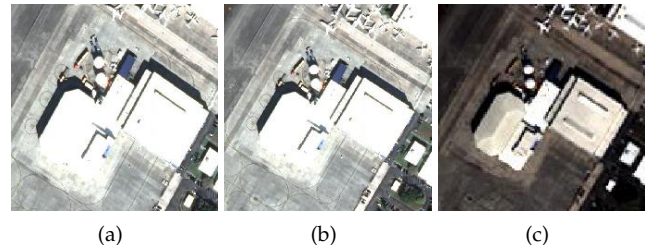


Fig. 10. Different image crops used for training: (a) original bounding box and (b) expanded bounding box extracted from JPG pan-sharpened images, and (c) expanded bounding box extracted from JPG multi-spectral images.

4 EXPERIMENTAL RESULTS

4.1 FMOW dataset

In this section we report and compare the Hydra performance in the FMOW dataset. First, to visualize the benefits of using the Hydra framework, we show the accuracy of the trained CNNs (body and heads) over the epochs in Figure 11. We also show the ensemble accuracy when the heads are available. In this experiment, we use the entire training subset and false detections of the evaluation subset for training, and the remaining images of the evaluation subset for accuracy computation. As can be observed, the body of the Hydra provides a good starting point for its

TABLE 2

Hydra’s heads description. For each head are given the network architecture, image crop style, augmentation technique and class weighting method. Three different image crop styles were considered: ORIG-PAN (Figure 10(a)), EXT-PAN (Figure 10(b)) and EXT-MULTI (Figure 10(c)). Augmentation techniques included random flips in vertical and horizontal directions (Flip), random zooming (Zoom) and random shifts (Shift). Class weighting methods were: no weighting, FMOw weights (Figure 3) and frequency-based weighting using the balanced heuristic [18] before (Frequency #2) and after (Frequency #1) a manual adjustment.

| Head | CNN | Crop | Augment | Class weighting |
|------|----------|-----------|---------|-----------------|
| #1 | DenseNet | EXT-PAN | Flip | Unweighted |
| #2 | DenseNet | ORIG-PAN | Flip | Frequency #1 |
| #3 | DenseNet | EXT-MULTI | Flip | Frequency #1 |
| #4 | DenseNet | EXT-PAN | Zoom | Frequency #2 |
| #5 | DenseNet | EXT-PAN | Shift | Unweighted |
| #6 | DenseNet | EXT-MULTI | Shift | FMOw weights |
| #7 | DenseNet | EXT-PAN | Flip | Frequency #2 |
| #8 | DenseNet | ORIG-PAN | Flip | Frequency #2 |
| #9 | ResNet | EXT-PAN | Flip | Unweighted |
| #10 | ResNet | EXT-MULTI | Flip | Frequency #1 |
| #11 | ResNet | ORIG-PAN | Flip | Frequency #1 |
| #12 | ResNet | EXT-MULTI | Flip | Frequency #2 |

heads, which have slightly different accuracy in the end of the training process. When the heads are combined, the obtained accuracy is considerably higher than the accuracy of the best performing head.

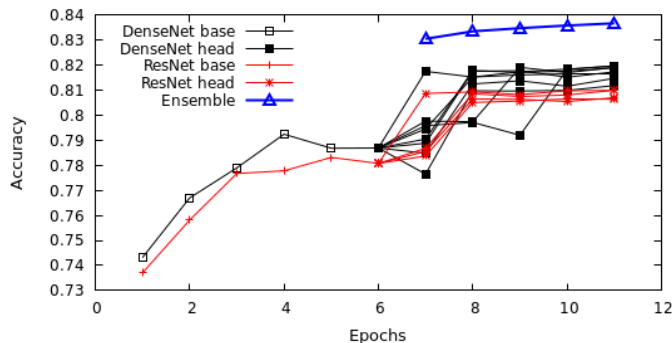


Fig. 11. Evaluation of the ensemble accuracy. The first six 6 epochs show the accuracy of the Hydra’s body using DenseNet and ResNet. The following epochs show the accuracy for each head separately as well as for the fusion of all heads (ensemble).

The confusion matrix for the best ensemble result in Figure 11 (epoch 11) is presented on Figure 12. The hardest classes for Hydra were: **shipyard** (mainly confused with **port**), **hospital** (confused with **educational institution**), **multi unit residential** (confused with **single unit residential**), **police station** (confused with **educational institution**), and **office building** (confused with **fire station**, **police station**, etc). We also had high confusion between **nuclear powerplant** and **port**, between **prison** and **educational institution**, between **space facility** and **border checkpoint**, and between **stadium** and **recreational facility**. These, however, are natural mistakes that could easily be repeated by human experts. Most of these classes look alike in aerial images (e.g. **shipyard** and **port**) or have similar features that can trick an automatic classifier (e.g. both **stadium** and **recreational facility** have a sport court). In Figure 13 we show examples of mislabeled regions that cannot be easily identified, even by a human.

We then reran the training process using all images from the training and evaluation subsets. The TopCoder submission system was used to obtain the \bar{F} -measure (Equation 1) for the testing subset, as it has no ground truth available so far. The obtained \bar{F} -measure is shown in Table 3 along with results reported by Christie *et al.* [1] and results for our best individual classifiers. As previously reported by Christie *et al.* [1], using metadata for classification purposes is better than just using the image information. In Table 3 we show that on-line data augmentation has also a big impact, increasing the accuracy of their respective versions without augmentation in more than 2%. Still, our ensemble can improve the performance even more, with a gap of at least 3% to all individual classifiers.

TABLE 3

\bar{F} -measure for the FMOw testing subset. Evaluated classifiers may use metadata information (M) and/or on-line data augmentation (O). \bar{F} -measure values for classifiers marked with † were reported by Christie *et al.* [1].

| | \bar{F} -measure |
|------------------------------------|--------------------|
| Hydra (DenseNet + ResNet) $_{M,O}$ | 0.781 |
| DenseNet $_{M,O}$ | 0.749 |
| ResNet $_{M,O}$ | 0.737 |
| LSTM $^{\dagger}_M$ | 0.734 |
| DenseNet $^{\dagger}_M$ | 0.722 |
| ResNet $_M$ | 0.712 |
| LSTM † | 0.688 |
| DenseNet † | 0.679 |

With this performance, we managed to finish the competition among the top ten competitors in the provisional scoreboard (5th place). We then submitted a dockerized version of Hydra, which was evaluated by the FMOw organizers using a sequestered dataset. As we show in Table 4, the Hydra ensemble was very stable, with nearly the same performance in the testing subset and sequestered dataset. Thanks to this, our final ranking was third place, with accuracy 1% lower than the best result achieved by another competitor.

TABLE 4

Final ranking: \bar{F} -measure for the top five participants of the FMOw challenge using the available testing subset (Open) and the sequestered dataset (Sequestered).

| Rank | Handle | Open | Sequestered |
|------|-------------------|--------|-------------|
| 1 | pfr | 0.7934 | 0.7917 |
| 2 | jianminsun | 0.7940 | 0.7886 |
| 3 | usf_bulls (Hydra) | 0.7811 | 0.7817 |
| 4 | zaq1xsw2tktk | 0.7814 | 0.7739 |
| 5 | prittm | 0.7681 | 0.7670 |

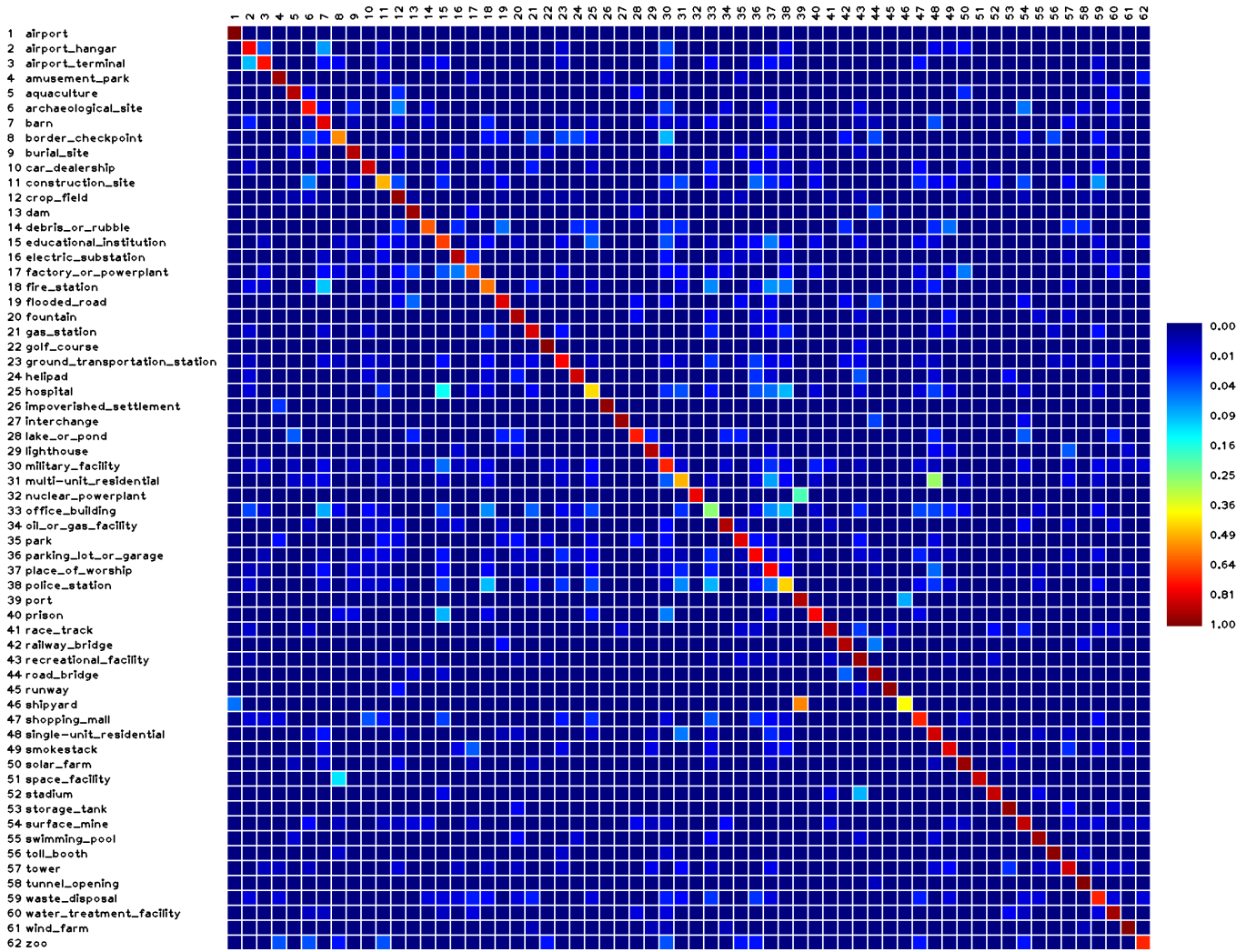


Fig. 12. Confusion matrix for the Hydra ensemble after 11 training epochs (Figure 11). Each row represents the ground truth label, while the column shows the label obtained by the Hydra. Large values outside of the main diagonal indicate that the corresponding classes are hard to be discriminated.

4.2 NWPU-RESISC45 dataset

We also reported the Hydra performance in the NWPU-RESISC45 dataset, which was recently compiled by Cheng *et al.* [4]. This dataset has 45 classes, with 700 images per class, each one with resolution of 256×256 pixels, totaling 31,500 images. The intersection of classes between FMOW and NWPU-RESISC45 is reasonable, with some land uses being overcategorized in NWPU-RESISC45 (e.g. **basketball court**, **baseball diamond** and **tennis court** are all labeled as **recreational facility** in the FMOW dataset) and some classes not representing land use, such as objects (e.g. **airplane** and **ship**) and vegetation (e.g. **desert**, **forest** and **wetland**). This dataset does not provide satellite metadata.

We followed the experimental setup proposed by Cheng *et al.* [4] and randomly chose 10% or 20% of the samples in each class for training. The remaining samples were used for testing. We repeated this experiment five times for each configuration, and reported the average accuracy and standard deviation. As can be shown in Table 5, Cheng *et al.* [4] compared six classifiers based on hand-crafted features and three different CNN architectures. In

their experiments, the best performance was achieved by a VGG16 network [10] that was trained using ImageNet weights as a starting point.

The configuration of the Hydra was slightly different in this experiment. We used 4 DenseNets and 4 ResNets, which were trained for 16 epochs (8 for the body and 8 for the heads). Each head for each architecture has a different augmentation: 1) no augmentation; 2) random vertical and horizontal flips; 3) random zooming; and 4) random shifts. The accuracy results for the NWPU-RESISC45 dataset are shown in Table 5. As NWPU-RESISC45 is less challenging than FMOW, the results are higher and the improvements are lower. The on-line data augmentation increased ResNet and DenseNet accuracies in about 1.0% and 1.6%, respectively. Individual classifiers for both architectures outperformed all previous results reported by Cheng *et al.* [4], and the Hydra ensemble was able to achieve the highest accuracy. The improvement on accuracy, however, was slightly greater than 1% when compared to individual CNNs. It is worth noting that we outperformed the best accuracy results reported by Cheng *et al.* [4] by more than 4%.

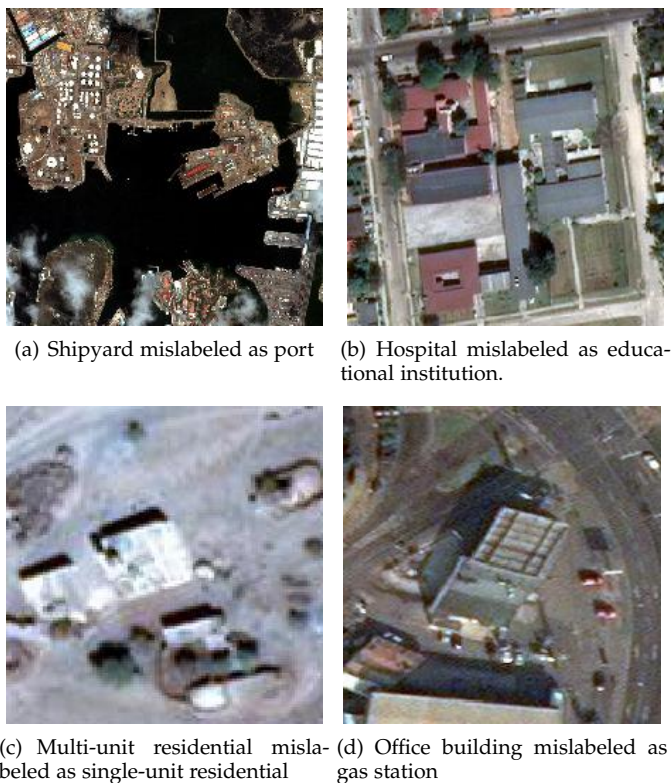


Fig. 13. Regions from the evaluation subset that were mislabeled by our Hydra ensemble.

TABLE 5

Accuracy for the NWPU-RESISC45 dataset using training/testing splits of 10%/90% and 20%/80%. Average accuracy and standard deviation were reported by using five different random splits. Evaluated classifiers may use on-line data augmentation (*O*) and/or ImageNet weights (*I*). Accuracy values for classifiers marked with † were reported by Cheng *et al.* [4].

| | Accuracy | |
|---|---------------------|---------------------|
| | 10%/90% | 20%/80% |
| Hydra (DenseNet + ResNet) _{<i>O,I</i>} | 92.44 ± 0.34 | 94.51 ± 0.21 |
| DenseNet _{<i>O,I</i>} | 91.06 ± 0.61 | 93.33 ± 0.55 |
| ResNet _{<i>O,I</i>} | 89.24 ± 0.75 | 91.96 ± 0.71 |
| VGG16 _{<i>I</i>} [†] | 87.15 ± 0.45 | 90.36 ± 0.18 |
| AlexNet _{<i>I</i>} [†] | 81.22 ± 0.19 | 85.16 ± 0.18 |
| GoogleNet _{<i>I</i>} [†] | 82.57 ± 0.12 | 86.02 ± 0.18 |
| AlexNet [†] | 76.69 ± 0.21 | 79.85 ± 0.13 |
| VGG16 [†] | 76.47 ± 0.18 | 79.79 ± 0.15 |
| GoogleNet [†] | 76.19 ± 0.38 | 78.48 ± 0.26 |
| BoVW [†] | 41.72 ± 0.21 | 44.97 ± 0.28 |
| LLC [†] | 38.81 ± 0.23 | 40.03 ± 0.34 |
| BoVW + SPM [†] | 27.83 ± 0.61 | 32.96 ± 0.47 |
| Color histograms [†] | 24.84 ± 0.22 | 27.52 ± 0.14 |
| LBP [†] | 19.20 ± 0.41 | 21.74 ± 0.18 |
| GIST [†] | 15.90 ± 0.23 | 17.88 ± 0.22 |

5 DISCUSSION

There is an extensive literature on algorithms for geospatial land image processing — often called remote sensing image processing. This broad and active field of research has many branches, such as semantic segmentation [29], [30], [31], [32], [33], target location [34] and region classification [35], [36], [37], [38], [39]. An exhaustive literature review was carried out by Cheng and Han [40] and covered most of the literature works based on handcrafted features. However, as can be seen in Table 5, handcrafted approaches are no longer competitive due to the recent advances on deep learning.

The FMOW challenge is focused on the classification branch and currently constitutes the most difficult task of its kind (63 classes, 470086 images). Other smaller datasets, such as UC Merced Land Use Dataset [2] (UCMerced, 21 classes, 2100 images), WHU-RS19 [3] (19 classes, 950 image), Brazilian Coffe Scenes [41] (BCS, 2 class, 2876 images) and Aerial Image Dataset *et al.* [42] (AID, 30 classes, 10000 images), were used in the literature but not necessarily represent a challenging task (*i.e.* reported results are reaching a nearly perfect score). Even NWPU-RESISC45 [4] (45 classes, 31500 images), the most recent dataset other than FMOW, is not as challenging. We were able to achieve nearly 95% accuracy using only 20% of its images for training. In comparison, the training/testing split for FMOW is about 85%/15%, but the top performance achieved by a competitor was still below 80%.

Anyway, there is no doubt that deep CNNs are becoming more and more popular for land use classification. Nogueira *et al.* [38] compared different state-of-the-art CNN architectures, such as AlexNet [19], GoogleNet [22] and VGG [10], and evaluated different training setups, such as using ImageNet weights as starting point and Support Vector Machines (SVM) for classification. They reported results for UCMerced, WHU-RS19 and BCS datasets, which were very successful when compared to many other approaches based on handcrafted features. Chaib *et al.* [39] improved regular VGG networks [10] by fusing the output of the last two fully connected layers. The work was validated using UCMerced, WHU-RS19 and AID. We also have CNN-based results reported by Christie *et al.* [1] and Cheng *et al.* [4] for NWPU-RESISC45 and FMOW datasets, respectively, as shown in Tables 3 and 5. Thus, CNN classifiers were definitely the best choice for our Hydra framework. After experimenting different architectures, we ended up using DenseNets and ResNets. The main reasons are that they perform better than previously mentioned architectures, have a reasonable level of complementarity, and achieve similar classification results.

In terms of computational resources consumption, Hydra has some disadvantages when compared to individual classifiers. If N heads are used, its training and inference costs tend to be $N/2$ and N times more expensive, respectively. On the other hand, when compared to other ensemble techniques with the same number of classifiers, Hydra’s training is approximately two times faster because half of the epochs are carried out for the Hydra’s body only.

Overall, the Hydra framework was a good fit to the FMOW restrictions described in Section 2.3. The time limit for testing was large enough to allow using many classi-

fiers, making the training time to generate them the main problem. Hydra succeeded in increasing the number of classifiers for inference without losing complementarity, a key requirement for ensembles. As a consequence, we finished the competition in the third place, with accuracy 1% lower than the best result achieved by another competitor.

6 CONCLUSIONS

Automatic and robust classification of aerial scenes is critical for decision-making by governments and intelligence/military agencies in order to support fast disaster response. This research problem, although extensively addressed by many authors, is far from being solved, as evidenced by the final results of the FMOw challenge.

The main contribution of this work was the development of a framework that automatically creates ensembles of CNNs to perform land use classification in satellite images. We called this framework Hydra due to its training procedure: the Hydra's body is a CNN that is coarsely optimized and then fine tuned multiple times to form the Hydra's heads. The resulting ensemble achieved the fifth best performance for the open testing subset of the FMOw challenge, qualifying our solution to the second phase of the competition. Then, the same ensemble was applied to a sequestered testing set that was used to officially rank the competitors, and it obtained the third best performance. Given that there were more than 50 active participants, including teams and individuals from academia and industry, and most of them probably were experimenting different CNN-based setups, we believe that Hydra is well aligned with the most recent state-of-the-art developments.

ACKNOWLEDGMENTS

Part of the equipments used in this project are supported by a grant (CNS-1513126) from the National Science Foundation (NSF) of USA. The Titan Xp used for this research was donated by the NVIDIA Corporation.

REFERENCES

- [1] G. Christie, N. Fendley, J. Wilson, and R. Mukherjee, "Functional map of the world," *arXiv preprint arXiv:1711.07846*, 2017.
- [2] Y. Yang and S. Newsam, "Bag-of-visual-words and spatial extensions for land-use classification," in *Proceedings of the 18th SIGSPATIAL International Conference on Advances in Geographic Information Systems*, ser. GIS '10. ACM, 2010, pp. 270–279.
- [3] D. Dai and W. Yang, "Satellite image classification via two-layer sparse coding with biased image representation," *IEEE Geoscience and Remote Sensing Letters*, vol. 8, no. 1, pp. 173–176, 2011.
- [4] G. Cheng, J. Han, and X. Lu, "Remote sensing image scene classification: Benchmark and state of the art," *Proceedings of the IEEE*, vol. 105, no. 10, pp. 1865–1883, Oct 2017.
- [5] H. Li, L. Jing, Y. Tang, Q. Liu, H. Ding, Z. Sun, and Y. Chen, "Assessment of pan-sharpening methods applied to worldview-2 image fusion," in *IEEE International Geoscience and Remote Sensing Symposium (IGARSS)*, 2015, pp. 3302–3305.
- [6] D. M. W. Powers, "Evaluation: From precision, recall and f-measure to roc., informedness, markedness & correlation," *Journal of Machine Learning Technologies*, vol. 2, no. 1, pp. 37–63, 2011.
- [7] G. Huang, Z. Liu, L. van der Maaten, and K. Q. Weinberger, "Densely connected convolutional networks," in *IEEE Conference on Computer Vision and Pattern Recognition (CVPR)*, 2017, pp. 4700–4708.
- [8] D. P. Kingma and J. Ba, "Adam: A method for stochastic optimization," *CoRR*, vol. abs/1412.6980, 2014.
- [9] H. Li, Z. Lin, X. Shen, J. Brandt, and G. Hua, "A convolutional neural network cascade for face detection," in *IEEE Conference on Computer Vision and Pattern Recognition (CVPR)*, 2015, pp. 5325–5334.
- [10] K. Simonyan and A. Zisserman, "Very deep convolutional networks for large-scale image recognition," pp. 1–14, 2015.
- [11] C. Ding and D. Tao, "Trunk-branch ensemble convolutional neural networks for video-based face recognition," *IEEE Transactions on Pattern Analysis and Machine Intelligence (TPAMI)*, vol. PP, no. 99, pp. 1–11, 2017.
- [12] T. G. Dietterich, *Ensemble Methods in Machine Learning*. Berlin, Heidelberg: Springer Berlin Heidelberg, 2000, pp. 1–15.
- [13] A. J. Sharkey, Ed., *Combining Artificial Neural Nets: Ensemble and Modular Multi-Net Systems*, 1st ed. Secaucus, NJ, USA: Springer-Verlag New York, Inc., 1999.
- [14] K. He, X. Zhang, S. Ren, and J. Sun, "Deep residual learning for image recognition," in *IEEE Conference on Computer Vision and Pattern Recognition (CVPR)*, 2016.
- [15] J. Deng, W. Dong, R. Socher, L.-J. Li, K. Li, and L. Fei-Fei, "ImageNet: A Large-Scale Hierarchical Image Database," in *IEEE Conference on Computer Vision and Pattern Recognition (CVPR)*, 2009.
- [16] A. Krogh and J. Vedelsby, "Neural network ensembles, cross validation and active learning," in *International Conference on Neural Information Processing Systems (NIPS)*, 1994, pp. 231–238.
- [17] A. Chandra and X. Yao, "Evolving hybrid ensembles of learning machines for better generalisation," *Neurocomputing*, vol. 69, no. 7, pp. 686–700, 2006.
- [18] G. King and L. Zeng, "Logistic regression in rare events data," *Political Analysis*, vol. 9, pp. 137–163, 2001.
- [19] A. Krizhevsky, I. Sutskever, and G. E. Hinton, "Imagenet classification with deep convolutional neural networks," *Commun. ACM*, vol. 60, no. 6, pp. 84–90, May 2017.
- [20] A. G. Howard, "Some improvements on deep convolutional neural network based image classification," *CoRR*, vol. abs/1312.5402, 2013. [Online]. Available: <http://arxiv.org/abs/1312.5402>
- [21] K. He, X. Zhang, S. Ren, and J. Sun, "Spatial pyramid pooling in deep convolutional networks for visual recognition," *IEEE Transactions on Pattern Analysis and Machine Intelligence (TPAMI)*, vol. 37, no. 9, pp. 1904–1916, 2015.
- [22] C. Szegedy, W. Liu, Y. Jia, P. Sermanet, S. Reed, D. Anguelov, D. Erhan, V. Vanhoucke, and A. Rabinovich, "Going deeper with convolutions," in *IEEE Computer Vision and Pattern Recognition (CVPR)*, 2015, pp. 1–9.
- [23] E. Ahmed, M. Jones, and T. K. Marks, "An improved deep learning architecture for person re-identification," in *IEEE Conference on Computer Vision and Pattern Recognition (CVPR)*, 2015, pp. 3908–3916.
- [24] K. Chatfield, K. Simonyan, A. Vedaldi, and A. Zisserman, "Return of the devil in the details: Delving deep into convolutional nets." in *British Machine Vision Conference (BMVC)*. BMVA Press, 2014.
- [25] T. DeVries and G. W. Taylor, "Dataset Augmentation in Feature Space," *ArXiv e-prints*, 2017.
- [26] L. Perez and J. Wang, "The Effectiveness of Data Augmentation in Image Classification using Deep Learning," *ArXiv e-prints*, Dec. 2017.
- [27] S. C. Wong, A. Gatt, V. Stamatescu, and M. D. McDonnell, "Understanding data augmentation for classification: When to warp?" in *International Conference on Digital Image Computing: Techniques and Applications*, 2016, pp. 1–6.
- [28] A. J. Ratner, H. R. Ehrenberg, J. D. Zeshan Hussain, and C. Re, "Learning to compose domain-specific transformations for data augmentation," in *International Conference on Neural Information Processing Systems (NIPS)*, 2017, pp. 1–11.
- [29] Q. Shi, B. Du, and L. Zhang, "Spatial coherence-based batch-mode active learning for remote sensing image classification," *IEEE Transactions on Image Processing (TIP)*, vol. 24, no. 7, pp. 2037–2050, 2015.
- [30] H. Lee and H. Kwon, "Going deeper with contextual cnn for hyperspectral image classification," *IEEE Transactions on Image Processing (TIP)*, vol. 26, no. 10, pp. 4843–4855, 2017.
- [31] H. Wu and S. Prasad, "Semi-supervised deep learning using pseudo labels for hyperspectral image classification," *IEEE Transactions on Image Processing (TIP)*, vol. 27, no. 3, pp. 1259–1270, 2018.
- [32] J. Zhao, Y. Zhong, H. Shu, and L. Zhang, "High-resolution image classification integrating spectral-spatial-location cues by conditional random fields," *IEEE Transactions on Image Processing (TIP)*, vol. 25, no. 9, pp. 4033–4045, 2016.

- [33] X. Xu, W. Li, Q. Ran, Q. Du, L. Gao, and B. Zhang, "Multisource remote sensing data classification based on convolutional neural network," *IEEE Transactions on Geoscience and Remote Sensing*, vol. PP, no. 99, pp. 1–13, 2017.
- [34] Z. Zou and Z. Shi, "Random access memories: A new paradigm for target detection in high resolution aerial remote sensing images," *IEEE Transactions on Image Processing (TIP)*, vol. 27, no. 3, pp. 1100–1111, 2018.
- [35] Y. Xia, L. Zhang, Z. Liu, L. Nie, and X. Li, "Weakly supervised multimodal kernel for categorizing aerial photographs," *IEEE Transactions on Image Processing (TIP)*, vol. 26, no. 8, pp. 3748–3758, 2017.
- [36] E. Li, J. Xia, P. Du, C. Lin, and A. Samat, "Integrating multilayer features of convolutional neural networks for remote sensing scene classification," *IEEE Transactions on Geoscience and Remote Sensing*, vol. 55, no. 10, pp. 5653–5665, 2017.
- [37] X. Lu, X. Zheng, and Y. Yuan, "Remote sensing scene classification by unsupervised representation learning," *IEEE Transactions on Geoscience and Remote Sensing*, vol. 55, no. 9, pp. 5148–5157, 2017.
- [38] K. Nogueira, O. A. Penatti, and J. A. dos Santos, "Towards better exploiting convolutional neural networks for remote sensing scene classification," *Pattern Recognition - Elsevier*, vol. 61, pp. 539–556, 2017.
- [39] S. Chaib, H. Liu, Y. Gu, and H. Yao, "Deep feature fusion for vhr remote sensing scene classification," *IEEE Transactions on Geoscience and Remote Sensing*, vol. 55, no. 8, pp. 4775–4784, 2017.
- [40] G. Cheng and J. Han, "A survey on object detection in optical remote sensing images," *ISPRS Journal of Photogrammetry and Remote Sensing - Elsevier*, vol. 117, pp. 11–28, 2016.
- [41] O. A. B. Penatti, K. Nogueira, and J. A. dos Santos, "Do deep features generalize from everyday objects to remote sensing and aerial scenes domains?" in *IEEE Conference on Computer Vision and Pattern Recognition Workshops (CVPRW)*, 2015, pp. 44–51.
- [42] G. S. Xia, J. Hu, F. Hu, B. Shi, X. Bai, Y. Zhong, L. Zhang, and X. Lu, "Aid: A benchmark data set for performance evaluation of aerial scene classification," *IEEE Transactions on Geoscience and Remote Sensing*, vol. 55, no. 7, pp. 3965–3981, 2017.